Mapping internal temperatures during high-rate battery applications

Paul Shearing (p.shearing@ucl.ac.uk)
UCL https://orcid.org/0000-0002-1387-9531
Thomas Heenan
UCL
Isabella Mombrini
ESRF
Alice Llewellyn
UCL
Stefano Checchia
https://orcid.org/0000-0003-0499-4885
Chun Tan
UCL
michael johnson
UCL
Anmol Jnawali
UCL
Gaston Garbarino
European Synchrotron Radiation Facility https://orcid.org/0000-0003-4780-9520
Rhodri Jervis
UCL
Dan Brett
University College London https://orcid.org/0000-0002-8545-3126
Marco Di Michel
ESRF - The European Synchrotron

Physical Sciences - Article

Keywords:

Posted Date: July 13th, 2022

DOI: https://doi.org/10.21203/rs.3.rs-1814550/v1

Mapping internal temperatures during high-rate battery applications

T. M. M. Heenan[1,2] , I. Mombrini[1,3], A. Llewellyn[1], S. Checchia[3], C. Tan[1,2], M. Johnson[1], A. Jnawali[1], Gaston Garbarino[3], R. Jervis[1,2], D. J.L. Brett[1,2], M. Di Michiel[3], P. R. Shearing[1,2,Ψ]

Electric vehicles (EV) demand high charge/discharge rates creating potentially dangerous temperature rises. Lithium-ion cells are sealed during their manufacture, making internal temperatures challenging to probe[1]. Tracking current collector expansion using X-ray diffraction (XRD) permits non-destructive internal temperature measurements[2]; however, cylindrical cells are known to experience complex internal strain[3,4]. Here, we characterise the state-of-charge (SoC), mechanical strain, and temperature within Lithium-ion 18650 cells operated at high rates (>3C) via two advanced synchrotron XRD methods: firstly, as entire cross-sectional temperature maps during open-circuit cooling and secondly, single-point temperatures during charge/discharge cycling. We observed that a 20-minute discharge on an energy-optimised cell (3.5 Ah) resulted in internal temperatures >70 °C, whereas, a faster 12-minute discharge on a power-optimised cell (1.5 Ah) resulted in substantially lower temperatures (< 50 °C). However, when comparing the two cells under the same electrical current, the peak temperatures were similar, e.g., a 6A discharge resulted in 40°C peak temperatures for both cell types. We observe that the *operando* temperature rise is due to heat accumulation, strongly influenced by the charging protocol e.g., constant-current (CC) and/or constant-voltage (CV). Design mitigations for temperature-related battery issues should now be explored using this novel methodology to provide opportunities for improved thermal management during high-rate EV applications.

Introduction

The electrification of transport will depend heavily on the improvement of lithium-ion (Li-ion) battery technologies. For example, aviation demands very high discharge rates during flight take-off[5], and similarly, extreme fast charging of automotive vehicles will be required to mitigate charging-point congestion and downtime for goods transport[6]. To meet these demands many high-rate solutions are emerging[7-9], however, thermally induced degradation remains problematic[10,11]. To advance cell designs such that these degradation issues can be mitigated, we must be able to accurately quantify internal temperatures during operation. This is challenging because cells are sealed during their manufacture for protection from contamination[12] and short-circuit[13]. To non-destructively measure temperature, the thermal expansion of metals[14] such as the current collector[2] have been measured via X-ray diffraction (XRD), but to resolve internal temperatures directly has required modification of the cell to incorporate thermocouples[1].

Computed tomography (CT) methods allow non-destructive measurements to be resolved spatially[15] and has uncovered many complex distributions of strain[3] and SoC[4]. Recently XRD-CT has revealed unprecedented insights into the internal SoC distributions within Li-ion cells[16]. Alas, lattice changes due to thermal expansion are orders of magnitude lower than those associated with lithiation. For instance, a 10 °C temperature change in copper would result in 10^{-4} Å lattice expansion[2], whereas the lattice changes during lithium intercalation (or de-intercalation) of the cathode active material are three orders of magnitude greater[2] e.g., 10^{-1} Å. Therefore, SoC can be extracted without characterising the thermal and mechanical strain due to their negligible contributions, but resolving temperature requires mechanical and thermal strain deconvolution, and the greater the number of spatial dimensions that are resolved (e.g., 1, 2, 3D) the more complex this becomes.

[1] Electrochemical Innovation Lab, Department of Chemical Engineering, UCL, London WC1E 7JE, U.K.
[2] The Faraday Institution, Quad One, Harwell Science and Innovation Campus, Didcot, OX11 0RA, U.K.
[3] The European Synchrotron, 71 Avenue des Martyrs, 38000, Grenoble, France.
[Ψ] Corresponding author: Professor Paul R Shearing, p.shearing@ucl.ac.uk

Materials demand is set to expand rapidly with the electrification of transport[17] and two contrasting cathode chemistries are lithium iron phosphate (i.e., LFP or $Li_{1-x}FePO_4$) and the layered nickel-rich transition metal oxides (e.g., NMC811 or $Li_{1-x-y}Ni_{0.8}Mn_{0.1}Co_{0.1}O_2$). LFP boasts longer lifetimes and enhanced safety, ideal for power-optimised cells; whereas NMC offers higher volumetric and gravimetric energy densities, more suitable for energy-optimised cell designs[18]. Similarly, many commercial anodes are fabricated from either graphite (e.g., Gr or Li_xC_6, Li_xC_{12}, Li_xC_{18}), silicon (e.g., Si or Li_xSi_y), silicon-oxide (e.g., SiO or $Li_xSi_yO_z$), or a composite of the two (e.g., Gr-Si, Gr-SiO_z). Note that the oxygen content in Si electrodes is often not known, hence it is commonplace to denote the material SiO_z, where z may be zero or negligible[19]. Si offers very high theoretical specific capacities however Gr undergoes significantly less expansion during cycling, accompanied by reduced stress[20]. Therefore, a plethora of materials combinations will compose the global Li-ion battery market, but a comparison of these key materials, which represent examples of power- and energy-optimised cells, can produce a suitable overview.

Here, we explain two methods of non-destructive temperature measurements for commercial cylindrical cells (e.g., 18650 format) via monitoring of the expansion/contraction of the Cu current collector crystal structures from XRD. Firstly, full cross-sectional temperature maps can be generated from conducting XRD-CT, ideal for exploring spatial distributions at the end of charge or discharge (e.g., 2D maps). And secondly, a multi-channel-collimator (MCC) can be used to resolve the temperature within arbitrarily selected internal locations (e.g., 1D lines) for real-time quantifications during operation. This article focuses on two contrasting commercially available 18650 cells, one with a Ni-rich NMC811 cathode vs. Gr-SiO_i anode, and a second with an LFP cathode vs. a Gr anode. The subsequent sections will discuss validation of temperature quantifications without electrochemical operation (*ex situ*), then acquisition via XRD-CT (*in situ*), and MCC-XRD (*operando*).

Ex situ temperatures

Cylindrical 18650 cells are assembled as jellyrolls as seen in the laboratory X-ray attenuation CT cross-sectional image in **Fig. 1a,b**. A similar cross section can be produced (at a lower spatial resolution) by monitoring the metallic current collector lattice spacing[2] to calculate the temperature (**Fig. 1c**) and reconstructing a spatially resolved image using XRD-CT **(Fig. 1d,e)**. XRD-CT can accurately reconstruct only quantities which are invariant for rotation around the tomographic rotation axis, temperature maps can be obtained since the thermal induced strain is in most materials a scalar quantity. The result is a spatiotemporal map of the internal cell temperature. As a simple proof-of-concept experiment the authors first mapped the internal temperatures within two 18650 cells after heating within a furnace (without electrochemical operation). The internal temperatures are displayed within **Fig. 1** as cross-sectional slices taken from the same region-of-interest (RoI) within the cell as the cells cooled over the course of ca. 30 minutes.

The temperature quantifications calculated by fitting the data of the Cu d-spacing closely followed fittings based on Newton's law of cooling (**Fig. 1c,** and see methods), indicating a high level of confidence in the quantifications. To the authors' knowledge, this is the first report of a spatially resolved temperature map within a commercial 18650 Li-ion cell without disassembly or modification. We will now consider the far more complex determination of temperatures driven by electrochemical operation. Note that all error bars throughout this article indicate statistical errors (standard deviation), the precision error is ca. ± 3 °C throughout.

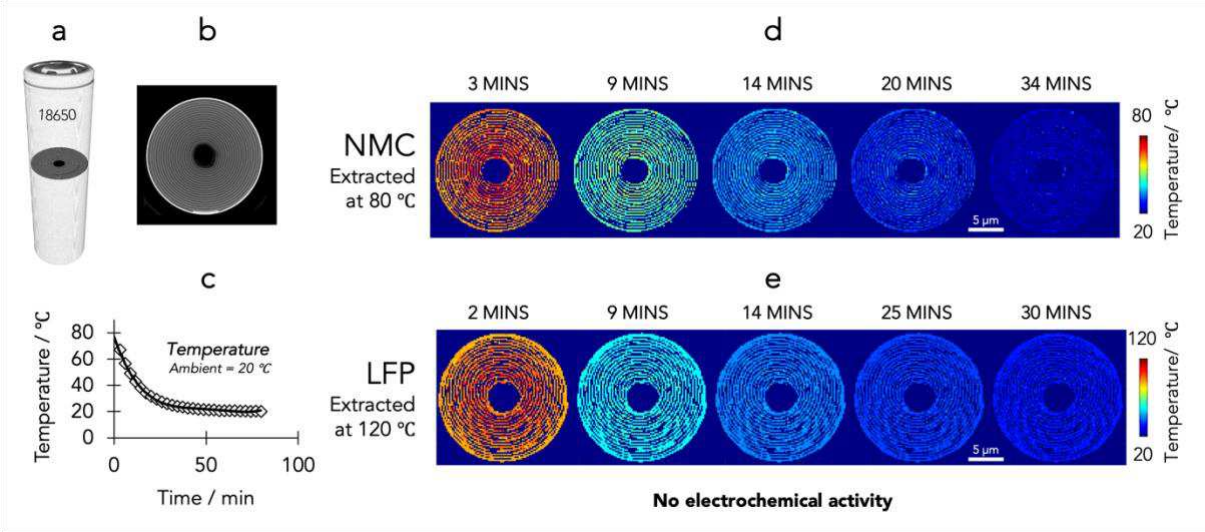

Fig 1. Spatiotemporal temperature mapping within 18650s without electrochemical operation. **a,b,** Laboratory X-ray CT (a) volume render and (b) ortho-slice of the NMC cell displaying the steel casing and internal jellyroll assembly. **c,** Internal temperatures within the NMC cell during cooling immediately after removal from the oven at 80 °C. **d,e,** A similar ortho-slice as shown in the laboratory CT (a) but instead representing the internal cell temperature obtained from synchrotron XRD-CT for (d) the NMC cell removed at 80 °C and (e) the LFP cell removed at 120 °C. Note that ambient temperature was assumed to be a consistent 20 °C.

In situ temperatures

To conduct electrochemical operation while also obtaining temperature measurements via XRD methods, a bespoke 18650 cell holder was designed and optimised to deliver sufficient XRD signal-to-noise (SNR) while also permitting high electrical currents with low circuit losses (**Fig. S1, S2**). Examples of the integrated XRD patterns and refinement can be found within the supplementary material (**Fig. S3**). Employing this set-up allowed both Coulomb counting of the electrochemical data and XRD analysis of the active electrode materials[2] to give indications of the SoC, and further, reconstruction via XRD-CT generated spatial maps of the SoC for each material[16]. In addition to SoC, mechanical strain information has proven highly important within 18650 cells[3,4,] and similar to SoC, XRD methods can also be used to extract this mechanical strain. Temperature measurements are the focus of this article but *operando* SoC and mechanical strain calculations can be found within the supplementary material (**Fig. S4-S9**).

As demonstrated for the oven-heating experiment (**Fig. 1**), internal temperatures could be mapped as 2D cross-sections as the cell cooled. **Fig. 2** displays the temperature values recorded during the transition to open circuit voltage (OCV) after discharge at various rates (approx. temperature peak values shown in **Fig. 2a**). To inspect peak internal thermal gradients the cell was divided into 8 radial zones (rings in **Fig. 2b**) but also compared to 8 azimuthal zones (segments in **Fig. 2c**). Increasing the C-rate from 1C to 3C increased the cell temperature by an additional ~ 40 ℃, which overshadowed the influence of any thermal gradients across the 8 radial (and azimuthal) zones, which were on the order of ±5 ℃; this was also true for the LFP cell (**Fig. S10**).

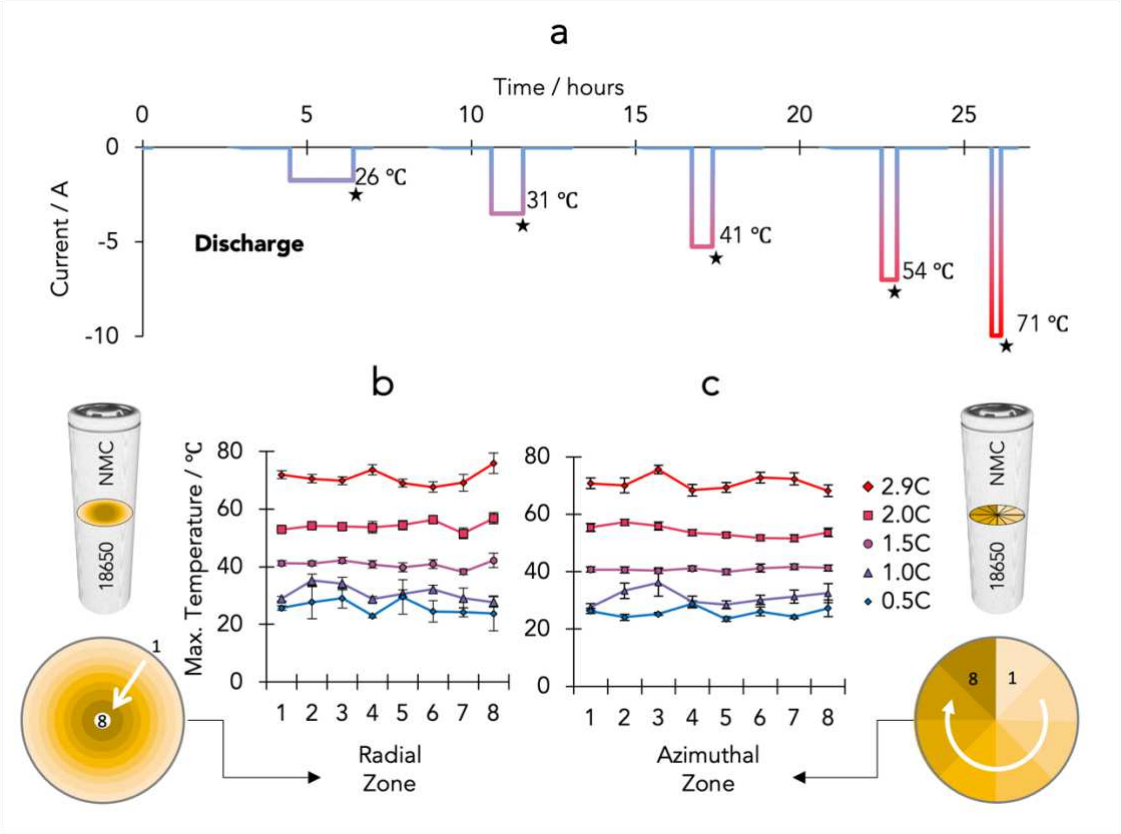

Fig. 2 ***In situ*** **internal temperature maps via XRD-CT. a,** The high-rate discharge currents for a commercial 18650 with measurement of the peak temperature during the open circuit transition (stars). **b,c,** Internal temperatures for 8 zones divided as (b) radial and (c) azimuthal zones. All error bars are statistical, precision error is ca. ± 3 °C throughout. Note that ambient temperature was assumed to be a consistent 20 °C.

Since the cell capacity dictates the electrical current for a particular C-rate, the contrasting power-optimised 18650 cell (LFP vs. Gr) was also assessed and compared to the energy-optimised counterpart (**Fig. 3a,b**), with the maximum temperature plotted with respect to the discharge current within **Fig. 3c** (circles) alongside two NMC cells (diamonds and triangles). The maximum temperature recorded grew similarly with discharge current irrespective of the cell type, e.g., at a discharge current of 6 A the maximum temperature was approximately 40 °C for all cells regardless of chemistry and this correlation held well throughout all discharge currents explored (i.e., up to approx. 10 A).

The thermal conductivities of the current collectors (assumed to be 398 and 235 W/m/K for copper and aluminium, respectively) are three orders of magnitude higher than the electrodes, and four orders higher than the separator. Therefore, it is unlikely that large amounts of heat are transferred rather through the electrodes or directly through the separator material. Instead, it is more probably that heat is preferentially and efficiently transferred around the jelly-roll winding through the metallic current collectors. Additionally, heat transfer from the interior to the exterior of the cell is very inefficient due to the much lower thermal conductivity of the steel case (~45 W/m/K). These factors explain the degree of homogeneity observed throughout the cell in **Fig. 2**, the current collector promotes temperature uniformity via high thermal conduction. Similarly, the strong dependence of the electrical current upon the peak temperature (**Fig. 3**) can be explained by the inefficient thermal properties of the casing design, which promotes heat accumulation, and the subsequent temperature rises. See further discussions within the Supplementary Material. This also indicates that Joule heating (at least for high currents) dominates heat generation, rather than reaction heating. Power-optimised LFP chemistries, with lower capacities, therefore present a favourable heat (and temperature) management option for high-rate applications since a lower relative electrical current can achieve a higher C-rate, thus faster charge/discharge and SoC change, although at the cost of lower energy densities. Therefore, if onboard energy density can be compromised, i.e., if shorter driving or flight ranges are acceptable in certain applications e.g.,

agricultural drones or warehouse robots, power-optimised cells such as these can offer improved thermal management.

The similarities of peak temperatures within the two cells at various discharge currents suggests that fundamental cell design alterations would be required to mitigate high temperatures (via improved heat dissipation) during high electrical currents, i.e., to enter the green 'target zone' visualised in **Fig 3c.** Consequently, the authors concluded that a method for understanding *operando* temperature changes (i.e., measurements during charge transfer) would be essential to explore how the heat is accumulated during operation.

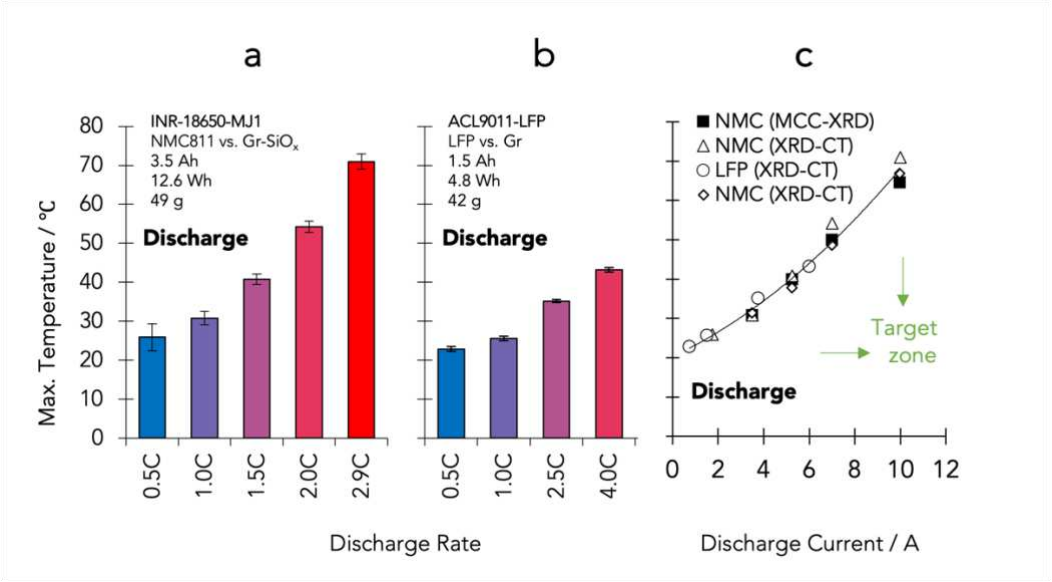

Fig. 3 ***In situ*** **internal temperature maxima via XRD-CT. a,b,** The internal temperature maxima within the commercial (a) energy- and (b) power-optimised cells immediately after discharge at various C-rates. **c,** The maximum internal temperature correlated with discharge current for two energy cells and one power cell, obtained at the end of discharge/start of OCV, via XRD-CT or MMC-XRD. Note that ambient temperature was assumed to be a consistent 20 °C.

Operando temperatures

During cell charge and discharge, in addition to thermal strain due to the Joule heating effect, the Cu current collector develops mechanical elastic strain caused by stress build up inside the cell, originated by different volumetric expansion/contraction of anode and cathode. To separate the mechanical from thermal strain and explore the temperature during stages that precede the peak temperatures reported in **Fig 3**, the methodology for a second XRD measurement was developed by employing a Multi-Channel Collimator (MCC) **(Fig. S11, S12**) which allows high speed (sub-second), high angular resolution and high SNR XRD measurements from a given spatial location (gauge volume). MCC-XRD measurements were performed along the same radial line, at two orthogonal orientations of the cell.

The *operando* MCC current collector tangential and radial strain measurements, combined with *operando* XRD-CT axial strain measurements permitted the analysis of temperature dynamics during the whole charge/discharge process, not only during open circuit. **Fig. 4** displays the temperature values recorded for zone 4 within an NMC cell during four charge-discharge cycles, whereby all four charges were conducted at 1C but each discharge was increased until the manufacturer's specified maximum electrical current of 10 A was reached. For completeness, **Fig. 3c** also reports the MCC data, showing close agreement with the XRD-CT values. The temperature and radial stress during the four charge profiles (at 1C, 3.5 A) were highly repeatable with minimal variation (**Fig. 4a,b**). Furthermore, the transition (dashed vertical line, ca. 45 mins) between the constant current (CC) and constant voltage (CV) stages was clearly distinguishable.

During CC the temperature rises due to the heat accumulation but once the current is allowed to decay under CV (or OCV) the temperature reduces, as heat loss to the surroundings exceeds that generated due to Joule heating. Consequently, there is a clear correlation between the electrical current employed and the temperature rise observed (as shown in **Fig. 4a**) but subsequently, the internal temperature at the end of charge will be dictated by the profile of the electrical current over the entire duration of the charge profile. For instance, other charging protocols such as current pulse or constant power may produce different temperature profiles to that seen here (under CC-CV) because the trade-off between heat generation and loss (to the surroundings) is different.

Discharge was conducted without a CV hold, i.e., only under CC. The temperature rise during the CC discharge followed a similar (but inverted) profile to the cooling after removal from the oven in the first experiment (compare heating in **Fig. 4a** to cooling in **Fig. 1d**); whereby initially the temperature changes rapidly but then slowing with time.

Naturally, unlike the thermal dynamics, the mechanical stress does not reduce during the CV stage due to the intercalation (and de- intercalation) mechanisms occurring during charge (**Fig. 4c**). This stress is only relieved once the discharge process is completed (**Fig. 4d**). Marginal stress hysteresis, observed as non-zero stress values at the end of discharge, may be attributed to the inaccessible discharge capacities at higher rates (**Fig. S9**). It should also be noted that stress was most dependent upon the SoC (see stress-capacity in **Fig. 4e,f**) and showed no correlation with C-rate (**Fig. 4f**).

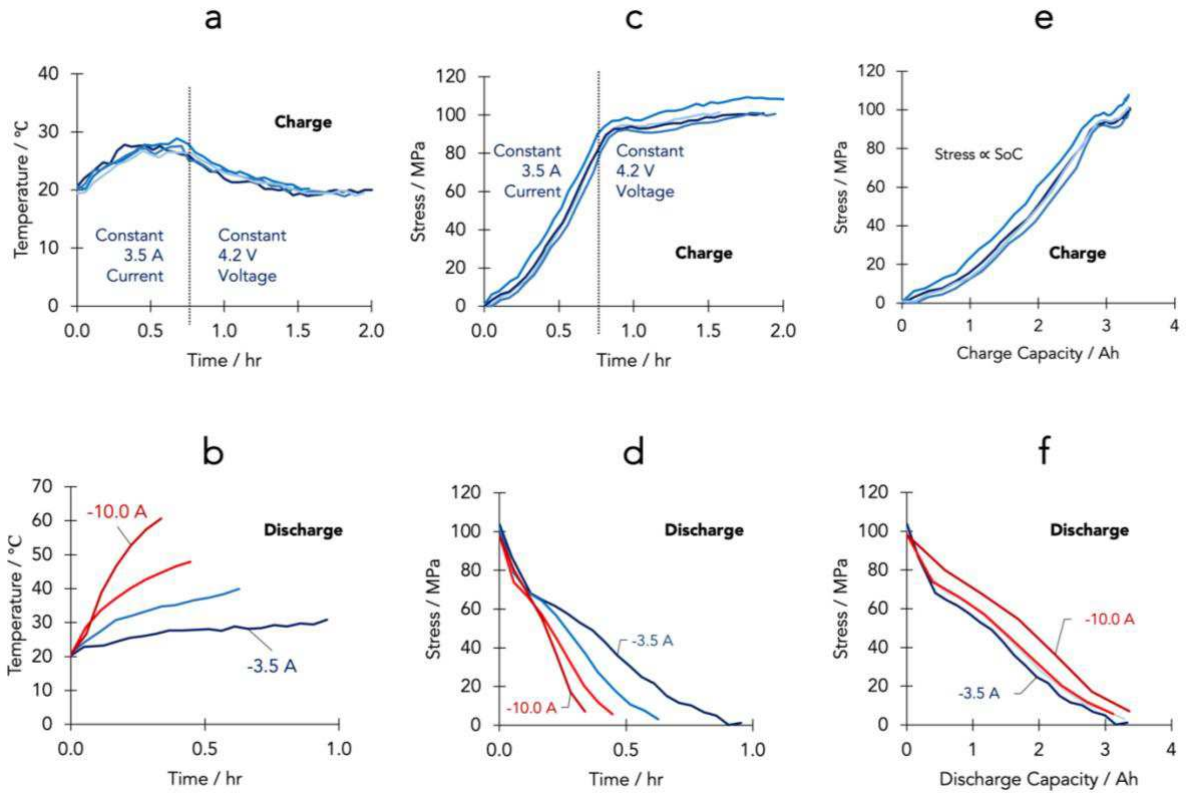

Fig. 4 ***Operando*** **internal temperatures via MCC-XRD. a,b,** The temperature during (a) charge and (b) discharge for the four cycles. **c,d,** The stress during (c) charge and (d) discharge for the four cycles. **e,f,** Assessing the relationship between the SoC (capacity) and the stress for the four (e) charge cycles all at 1C and (f) discharge cycles at various C-rates. Note that ambient temperature was assumed to be a consistent 20 °C.

Future thermal management

In conclusion, we present here two methodologies to accurately (± 3 °C) quantify internal temperatures during high-rate (up to 10.0 A) operation of commercial Li-ion 18650s without cell modification or disassembly. These methods should be applicable to the vast majority of, if not all, commercial 18650s, and may be conducted by any specialist XRD synchrotron beamline with the cell holder (described

within the methodology and supplementary) and using the correct imaging setup. Moreover, minor modifications would permit the study of other cell geometries, e.g., 2170 and 4680, and these options are currently being explored by the authors.

Temperature mapping using XRD-CT revealed that the peak temperatures reached within the cell are relatively homogeneous (spatially) at the end of discharge and the magnitude of this temperature peak is largely dictated by the electrical current employed. The MCC-XRD temperature mapping method then revealed that this temperature peak is reached due to an accumulation of heat and is strongly influenced by the charging protocol (e.g., the use of CC or CC-CV, etc.).

As imaging instruments advance, the spatial and temporal resolutions employed here may improve. Consequently, studies including other chemistries and cell microstructures may provide additional understanding behind the complex transport of heat during charge transfer. This presents new opportunities to study novel thermal management techniques with real-time quantifications that can inform computational modelling[21] and accelerate the design iteration process. The prediction and control of temperatures is a large industrial challenge that is expected to receive increased attention in coming years as the performance of batteries is advanced to meet application requirements[22]. Intelligent thermal management of Li-ion cells in combination with materials innovations[8,9] will reduce range-anxiety for automotive vehicles and aid aircraft take-off, ultimately enabling the transition to electrified transport.

References

1. Spinner, N., et al. Novel 18650 lithium-ion battery surrogate cell design with anisotropic thermophysical properties for studying failure events. Journal of Power Sources. Volume 312, Pages 1-11 (2016). https://doi.org/10.1016/j.jpowsour.2016.01.107

2. Yu, X., et al. Simultaneous Operando Measurements of the Local Temperature, State of Charge, and Strain inside a Commercial Lithium-Ion Battery Pouch Cell. J. Electrochem. Soc. 165 A1578 (2018). https://doi.org/10.1149/2.1251807jes

3. Kok, M., et al. Virtual unrolling of spirally-wound lithium-ion cells for correlative degradation studies and predictive fault detection. Sustainable Energy Fuels, 3, 2972-2976 (2019). https://doi.org/10.1039/C9SE00500E

4. Ziesche, R.F., Arlt, T., Finegan, D.P. et al. 4D imaging of lithium-batteries using correlative neutron and X-ray tomography with a virtual unrolling technique. Nat Commun 11, 777 (2020). https://doi.org/10.1038/s41467-019-13943-3

5. Sripad, S., Bills, A. & Viswanathan, V. A review of safety considerations for batteries in aircraft with electric propulsion. MRS Bulletin 46, 435–442 (2021). https://doi.org/10.1557/s43577-021-00097-1

6. Li, M., et al. Fast Charging Lithium-ion Batteries for a New Era of Electric Vehicles. Cell Reports Physical Science. Volume 1, Issue 10, 100212 (2020). https://doi.org/10.1016/j.xcrp.2020.100212

7. Tomaszewska, A., et al. Lithium-ion battery fast charging: A review. eTransportation. Volume 1, 100011 (2019). https://doi.org/10.1016/j.etran.2019.100011

8. Griffith, K.J., et al. Niobium tungsten oxides for high-rate lithium-ion energy storage. Nature 559, 556–563 (2018). https://doi.org/10.1038/s41586-018-0347-0

9. Billaud, J., et al. Magnetically aligned graphite electrodes for high-rate performance Lithium-ion batteries. Nat Energy 1, 16097 (2016). https://doi.org/10.1038/nenergy.2016.97

10. Lain, M. & Kendrick, E. Understanding the limitations of lithium ion batteries at high rates. Journal of Power Sources. Volume 493, 229690 (2021). https://doi.org/10.1016/j.jpowsour.2021.229690

11. Ma, S., et al. Temperature effect and thermal impact in lithium-ion batteries: A review. Progress in Natural Science: Materials International. Volume 28, Issue 6, Pages 653-666 (2018). https://doi.org/10.1016/j.pnsc.2018.11.002

12. Finegan, D., et al. Tracking Internal Temperature and Structural Dynamics during Nail Penetration of Lithium-Ion Cells. J. Electrochem. Soc. 164 A3285 (2017). https://doi.org/10.1149/2.1501713jes

13. Han, A., et al. Effect of Humidity on Properties of Lithium-ion Batteries. Int. J. Electrochem. Sci., 16, Article ID: 210554, (2021). https://doi.org/10.20964/2021.05.54

14. Hagart-Alexander, C. Instrumentation Reference Book (Fourth Edition), Chapter 21 - Temperature Measurement. Pages 269-326 (2010). https://doi.org/10.1016/B978-0-7506-8308-1.00021-8

15. Houx, J. L., Kramer, D. X-ray tomography for lithium ion battery electrode characterisation — A review. Energy Reports, Volume 7, Supplement 2, Pages 9-14 (2021). https://doi.org/10.1016/j.egyr.2021.02.063

16. Petz, D., et al. Lithium distribution and transfer in high-power 18650-type Lithium-ion cells at multiple length scales. Energy Storage Materials. Volume 41, Pages 546-553 (2021). https://doi.org/10.1016/j.ensm.2021.06.028

17. Xu, C., et al. Future material demand for automotive lithium-based batteries. Commun Mater 1, 99 (2020). https://doi.org/10.1038/s43246-020-00095-x

18. Ding, Y., et al. Automotive Lithium-ion Batteries: Current Status and Future Perspectives. Electrochem. Energ. Rev. 2, 1–28 (2019). https://doi.org/10.1007/s41918-018-0022-z

19. Heenan, T., et al. Identifying the Origins of Microstructural Defects Such as Cracking within Ni-Rich NMC811 Cathode Particles for Lithium-Ion Batteries. Advanced Energy Materials. Volume 10, Issue 47, 2002655 (2020). https://doi.org/10.1002/aenm.202002655

20. Finegan, D., et al. Spatially Resolving Lithiation in Silicon–Graphite Composite Electrodes via in Situ High-Energy X-ray Diffraction Computed Tomography. Nano Lett., 19, 6, 3811–3820 (2019). https://doi.org/10.1021/acs.nanolett.9b00955

21. Tranter, T., et al. Communication—Prediction of Thermal Issues for Larger Format 4680 Cylindrical Cells and Their Mitigation with Enhanced Current Collection. J. Electrochem. Soc. 167 160544 (2020). https://doi.org/10.1149/1945-7111/abd44f

22. Offer, G., et al. Cool metric for lithium-ion batteries could spur progress. Nature 582, 485-487 (2020). https://doi.org/10.1038/d41586-020-01813-8

Figure legends

Fig 1. Spatiotemporal temperature mapping within 18650s without electrochemical operation. a,b, Laboratory X-ray CT (a) volume render and (b) ortho-slice of the NMC cell displaying the steel casing and internal jellyroll assembly. **c,** Internal temperatures within the NMC cell during cooling immediately after removal from the oven at 80 °C. **d,e,** A similar ortho-slice as shown in the laboratory CT (a) but instead representing the internal cell temperature obtained from synchrotron XRD-CT for (d) the NMC cell removed at 80 °C and (e) the LFP cell removed at 120 °C. Note that ambient temperature was assumed to be a consistent 20 °C.

Fig. 2 *In situ* internal temperature maps via XRD-CT. a, The high rate discharge currents for a commercial 18650 with measurement of the peak temperature at the point of open circuit (stars). **b,c,** Internal temperatures for 8 zones divided as (b) radial and (c) azimuthal zones. All error bars are statistical, precision error is ca. ± 3 °C throughout. Note that ambient temperature was assumed to be a consistent 20 °C.

Fig. 3 *In situ* internal temperature maxima via XRD-CT. a,b The internal temperature maxima within the commercial (a) NMC and (b) LFP cells immediately after discharge at various C-rates. **c,** The max internal temperature correlated with discharge current for two NMC cells and the LFP cell, obtained at the start of open-circuit/end of discharge, obtained either via XRD-CT or MMC-XRD. Note that ambient temperature was assumed to be a consistent 20 °C.

Fig. 4 *Operando* internal temperatures via MCC-XRD. a,b, The temperature during (a) charge and (b) discharge for the four cycles. **c,d,** The stress during (c) charge and (d) discharge for the four cycles. **e,f,** Assessing the relationship between the SoC (capacity) and the stress for the four (e) charge cycles all at 1C and (f) discharge cycles at various C-rates. Note that ambient temperature was assumed to be a consistent 20 °C.

Methods

18650 Li-ion cells. The commercial cell testing was performed on 3.5 Ah nominal capacity LG Chem INR-18650-MJ1 cells (Nkon, Netherlands). These cells are assembled using nickel-rich ($LiNi_{0.8}Mn_{0.1}Co_{0.1}O_2$) cathodes and composite graphite-silicon anodes. Where stated, a comparison cell was also analysed: the 1.5 Ah nominal capacity ACL9011, composed of a lithium iron phosphate (LFP) cathode and graphite anode.

Laboratory X-ray CT. The lab X-ray CT data was collected using a Nikon XT H225 (Nikon Metrology, Inc. U.S.A.) by rotating the sample through 2,278 angular projections and exposing the sample at each increment to a polychromatic X-ray beam of characteristic peak energy of 58 keV (W-Kα), each with an exposure time of 1 s; with an isotropic 36 µm reconstructed voxel length. This data has been published openly elsewhere and is free to download[23]. All data was reconstructed using commercial software employing cone-beam filtered-back-projection (FBP) algorithms ("CT Pro 3D," Nikon Metrology, Inc. U.S.A.).

Laboratory data visualisation. All lab data was visualised using Avizo Fire software (Avizo, Thermo Fisher Scientific, Waltham, Massachusetts, U.S.A.). Volume renders and ortho-slice cross-sections were generated based upon the raw, unprocessed greyscale data within the tomogram.

Synchrotron. All synchrotron experiments were performed at the ID15A beamline[24] at the ESRF – The European Synchrotron, Grenoble, France. During the XRD-CT measurements the sample was continuously rotated while being translated horizontally across the X-ray beam path in steps defined by the horizontal beam size (**Fig. S1**). The MCC-XRD data was collected during translation of the sample along either the direction parallel to the beam (x) or perpendicular (y). In both setups the scattered signal was collected at rates of 200-250 Hz using a Pilatus 3X CdTe 2M detector (Dectris, Baden-Dättwil, Switzerland).

Multi-Channel Collimator (MCC). The MCC used in this work consists of two concentric sets of slits radially aligned around the centre of rotation of the diffractometer. The two sets of slits consist of tungsten carbide blades supported by a stainless-steel frame. They contain 75 slits, separated by 0.8°, with a distance of 50 and 200 mm respectively from the sample.[28] Thanks to this geometry it is possible to select the scattering signal from an internal volume in the sample (**Fig S11**). The gauge volume from which the diffraction signal is measured is given by the intersection of the primary X-ray beam with the volume seen by the detector through the MCC slits (**Fig S11**). The dimension of the gauge volume full-width-half-maximum (FWHM) along x axis (δx) is approximated by the formula as:

Equation 1
$$\delta x = \frac{a}{\left(1-\frac{r_1}{r_2}\right)\sin 2\theta} + \frac{\delta y}{\tan 2\theta},$$

Where, a = 50 µm is the width of the inner slits; r_1 and r_2 are the inner and outer slit radii, respectively; and δy is the horizontal beam size. As shown by equation 1, the gauge volume varies with the diffraction angle, 2θ. The gauge volume dimensions along *y* and *z* directions correspond to the X-ray beam cross section. Sample diffraction patterns without and with multichannel collimator are compared in **Fig.S12**.[28,29]

Commercial 18650 cell holder. All *in situ* and *operando* measurements were conducted using the same cell set-up (**Fig. S1, S2a**) during operational charge-discharge cycling (**Fig. S2b**), allowing crystallographic information to be resolved internally through various stages of operation. This holder was capable of handling up to 20 A of continuous electrical current, which should encompass the majority of commercial 18650 cell C-rate capabilities. Note that these experiments were limited to 10 A due to the potentiostat limit.

Electrochemistry. The cells were cycled using a Biologic SP300 cycler with 10 A booster (Biologic, France). The first XRD-CT experiments were conducted on an NMC cell discharged at: 0.5C (1.75 A), 1.0C (3.50 A), 1.5C (5.25 A), 2.0C (7.00 A), and 2.9C (9.96 A). The first charge was conducted at 0.5C (1.75 A) in order to begin the discharge experiments, all subsequent charges were conducted at 1.0C (3.5 A). After each charge or discharge step, the cell was held at OCV for 30 mins. This was repeated with a second NMC cell. The second XRD-CT experiment was conducted on an LFP cell discharged at: 0.5C (0.75 A), 1.0C (1.50 A), 2.5C (3.75 A), 4.0C (6.00 A), and 5.0C (7.50 A). The first charge was conducted at 0.5C (0.75 A) in order to begin the discharge experiences, all subsequent charges were conducted at 1.0C (1.5 A). After each charge or discharge step, the cell was held at OCV for 30 mins. The MCC-XRD experiment was conducted on an NMC cell discharged at: 1.0C (3.50 A), 1.5C (5.25 A), 2.0C (7.00 A), and 2.9C (9.96 A). The first charge was conducted at 0.5C (1.75 A) in order to begin the discharge experiences, all subsequent charges were conducted at 1.0C (3.5 A). After each charge or discharge step, the cell was held at OCV for 30 mins.

***Ex situ* temperatures.** The *ex situ* oven-heating experiments were performed using ultra-fast XRD-CT with an incident beam energy of 95 keV and a 200 x 200 μm^2 beam size. The detector-sample distance was set to 1000 mm. XRD-CT scans were performed every ~170 seconds . After keeping the LFP cell at 120 °C for three hours, XRD-CT data was collected over the course of 1.25 hours while the cell was cooling to room temperature with no electrochemistry applied. The same measurements were performed every ~255 seconds on an NMC811 cell, during cooling in air, after holding at 80 °C for three hours.

***In situ* temperature measurements.** The *in situ* OCV cooling experiments were performed using ultra-fast XRD-CT while charging and discharging the cell at different rates. The experiments were conducted using an X-ray beam of 100 keV and a 200 x 200 μm^2 size, XRDCT scans were performed every 3 minutes. The detector-sample distance was set to 1275 mm for NMC cells, and 1770 mm for LFP cells. XRD-CT datasets were collected continuously during charge/discharge for the entire electrochemical cycle on each cell. The cell mounted in the battery holder was connected to the Biologic SP300 potentiostat.

***Operando* temperature measurement.** The *operando* experiments were performed using MCC-XRD. These experiments employed an incident beam energy of 95 keV and a 200 × 25 (VxH) μm^2 beam size to attain a narrow gauge-volume. The cell, mounted in the battery holder, was connected to the Biologic SP300 potentiostat. The detector-sample distance was set to 1000 mm. The sample was translated alternately perpendicular and parallel to the incident beam, collecting multiple diffraction points to select different Cu current collector spirals in each scan.

XRD-CT reconstruction. For each measured XRD-CT slice, the 2D diffraction patterns $I(2\theta,\eta)$ from all rotation and translation positions were integrated over the azimuthal angle (η) using pyFAI software[25]. The azimuthal range was ±15° around the vertical scattering plane, corresponding to a condition where the momentum transfer vector ($\boldsymbol{q}$) is virtually parallel to the sample rotation axis (z, see **Fig. S1b**). The resulting azimuthally integrated data was corrected for incident flux and sample absorption effects and finally reconstructed through a FBP algorithm implemented in Matlab (Mathworks, Cambridge, U.K.).

Temperature calculations. To calculate internal cell temperatures, position of Cu Bragg peaks were calculated for each voxel in the tomograms and for each of the MCC scans. Peak centre of mass calculations gave accurate *d*-spacings for the available Cu reflections in the different sample/setup combinations used. To inspect internal thermal gradients, spatially resolved data were binned into eight circular regions inside the battery based on their radial position between the internal and the external border of the active area (**Fig. 2b**). Eight azimuthal regions were also defined as shown in **Fig.2c**. To reduce the statistical error, the mean values were calculated for each region as function of time. The temperature generated from the C-rate discharge applied to the cell in the 8 zones (radial and azimuthal) was calculated by fitting the data of Cu d-spacing from the end of the discharge until the end of the following rest based on Newton's law of cooling. Since the XRD-CT data were taken during OCV in

the discharge state, it was assumed that no strains were contributing to the contraction of the Cu crystal lattice during cooling. The function used for the fitting was an exponential decay:

Equation 2: $$\mathrm{d}(t) = \mathrm{d}_0 - \Delta\mathrm{d} \cdot \mathrm{e}^{-\frac{t-t_0}{\tau}}$$

Where t is the time, t_0 the time at which the discharge finished, τ the decay time, Δd the d-spacing variation of a given Bragg reflection of the Cu current collector, d_0 is the d-spacing at time t_0. Temperature variation ΔT inside the battery at the end of each discharge for the eight zones was calculated from the relative change in d-spacing using Equation 3. The thermal expansion coefficient of Cu was experimentally determined through temperature-dependent XRD on a fragment of the current collector extracted from a 18650 cell.

Equation 3: $$\Delta T = \frac{1}{\alpha}\frac{\Delta\mathrm{d}}{d_o}$$

Strain calculations. The positions of Cu Bragg peaks used for internal temperature calculations were also used to calculate strain values. Likewise, the battery section was split into eight radial zones and values from the voxels in each zone averaged for better statistics. Strain on Cu current collector caused by the volume change due to lithiation of graphite was calculated by measuring the Cu d-spacing before the charge (d_0) and the Cu d-spacing after the charge (d). The final strain after charge was calculated for the eight circular zones inside the battery with the following equation:

Equation 4: $$\varepsilon = \frac{d-d_0}{d_0}$$

Rietveld refinements. Rietveld analysis was performed on the $I(2\theta)$ patterns in the reconstructed tomograms of the cells to calculate the SoC from the varying distribution of lithiated anode phases. Batch fit routines were set up in Topas v7[26] to handle the analysis of the several thousands of diffractograms in each dataset. While the refinement strategy was unconstrained (i.e., letting structural parameters vary within a suitable range), care must be applied when setting parameter limits and initial values in order to ensure that the fit converges and avoids local minima. The fitted model comprised a 2-parameter Chebyshev polynomial background and four rhombohedral graphite-like phases (delithiated graphite and lithiation stages I, II, III). Each phase had refinable lattice parameters, scale factor and one peak-width parameter, whose $Tan(2\theta)$-dependent broadening was convoluted with a fixed Pseudo-Voigt contribution previously refined on the calibrant powder (NIST SRM 674b Cr_2O_3) to yield the final peak shape.

SoC calculations. The number of moles of Li per mole of C_6 was calculated from the mass fractions of the lithiation stages determined by Rietveld analysis.[27] The diffraction patterns were consistent with a choice of four stages: graphite, Stage III, Stage II, and Stage I. Stage III was considered as a solid solution whose Li content varied linearly with the lattice parameter c between LiC_{19} and LiC_{30}. The stoichiometries of Stage II and Stage I were LiC_{12} and LiC_6, respectively. The lithiation state x in Li_xC_6 was calculated as:

Equation 5: $$x = 6 \times \frac{\frac{\sum_{s=1}^{3} m_s f_s}{w_{Li}}}{\frac{m_g + \sum_{s=1}^{3} m_s(1-f_s)}{w_C}}$$

Here w_{Li} and w_C are the atomic weights of Li and C; m_g the mass fraction of graphite; m_s the mass fraction of phase s (lithiation stages I-III); f_s the mass fraction of Li in the same phases.

Methods references

23. Heenan, T. M.M., et al. Data for an Advanced Microstructural and Electrochemical Datasheet on 18650 Li-ion Batteries with Nickel-Rich NMC811 Cathodes and Graphite-Silicon Anodes. Data in Brief. Volume 32, 106033, (2020). https://doi.org/10.1016/j.dib.2020.106033

24. Vaughan, G.B.M., et al. ID15A at the ESRF - a beamline for high speed operando X-ray diffraction, diffraction tomography and total scattering. J. Appl. Cryst. 27, 515-528 (2020). https://doi.org/10.1107/S1600577519016813

25. Ashiotis, G., et al. The Fast Azimuthal Integration Python Library: PyFAI. J. Appl. Cryst. 48, 2, 510-519, (2015). https://doi.org/10.1107/S1600576715004306

26. Coelho, A. TOPAS and TOPAS-Academic: an optimization program integrating computer algebra and crystallographic objects written in C++. J. Appl. Cryst. 51, 210-218 (2018). https://doi.org/10.1107/S1600576718000183

27. Finegan, D., et al. Spatial dynamics of lithiation and lithium plating during high-rate operation of graphite electrodes. Energy Environ. Sci., 13, 2570-2584 (2020). https://doi.org/10.1039/d0ee01191f

28. Morad, G., et al. High efficiency multichannel collimator for structural studies of liquids and low-Z materials at high pressures and temperatures. Rev. Sci. Instrum. 82, 023904 (2011) https://doi.org/10.1063/1.3551988

29. Yaoita et al. Angle-dispersive diffraction measurement system for high-pressure experiments using a multichannel collimator. Rev. Sci. Instrum. 68 (5), (1997) https://doi.org/10.1063/1.1505104

Data and code availability

Correspondence and requests for materials should be addressed to the corresponding author: Professor Paul R Shearing.

Acknowledgements

This work was carried out with funding from the Faraday Institution (faraday.ac.uk; EP/S003053/1), grant number FIRG001 and FIRG003. The authors would like to acknowledge the Royal Academy of Engineering (CiET1718\59) for financial support. Use of the instruments was supported by EP/N032888/1. The ESRF is acknowledged for provision of beamtime (ME-1577: 10.15151/ESRF-ES-549494442, IH-MA-171: 10.15151/ESRF-ES-532206404, IH-MA-153: 10.15151/ESRF-ES-478854138). M.J acknowledges HORIBA-MIRA, UCL and EPSRC (EP/R513143/1) for a CASE studentship. The authors would like to thank Mohamed Mezoura (ESRF) for lending of the MCC and related equipment, and Dr. Partha Paul for beamline support.

Author contributions

TH led the investigation. TH, MM, PS conceived the experiments. TH, IM, AL, CT, SC, MM, M.J., A.J, GG performed the experiments, TH, IM, AL, CT, SC, MM, M.J., A.J, XX, YY, ZZ performed the data analysis. MM leads work at ESRF as the Scientist in Charge of ID15A. RJ leads work as the Degradation Project Manager for the Faraday Institution. PS and DB lead all work from the Electrochemical Innovation Lab (UCL) and sourced all funding to support this work.

Competing interest declaration

There are no competing interests known to the authors to declare.

Additional information

Supplementary information is available for this paper.

Corresponding author

Professor Paul R Shearing, p.shearing@ucl.ac.uk

Supplementary information

Mapping internal temperatures during high-rate battery applications

T. M. M. Heenan[1,2], I. Mombrini[1,3], A. Llewellyn[1], C. Tan[1,2], S. Checchia[3], M. Johnson[1], A. Jnawali[1], Gaston Garbarino[3], R. Jervis[1,2], D. J.L. Brett[1,2], M. Di Michiel[3], P. R. Shearing[1,2,Ψ]

Ψ Corresponding author: Professor Paul R Shearing, p.shearing@ucl.ac.uk

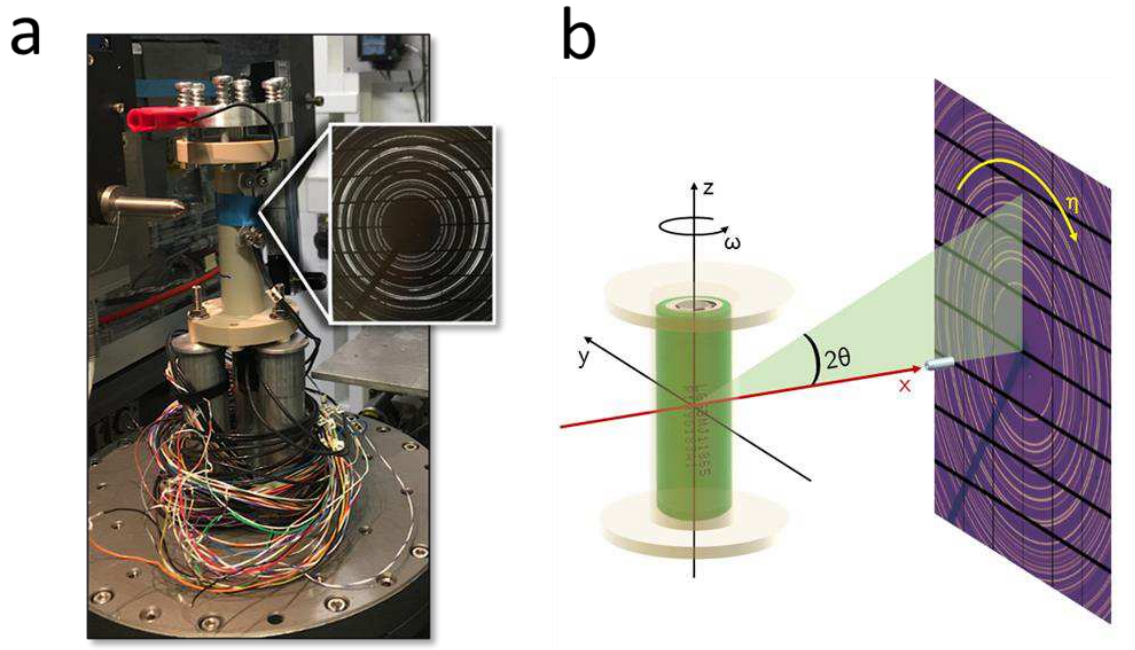

Fig S1. **Experimental set-up. a,** A photograph of the cell holder with electrical connections as mounted on the diffractometer at ID15A and an example of the X-ray diffraction rings collected from the cells. **b,** Example diagram of the sample-detector geometry used for all experiments: the x-ray beam is directed along x and normal to the detector plane; sample translation perpendicular to the beam goes along y; ω is the angle about the rotation axis.

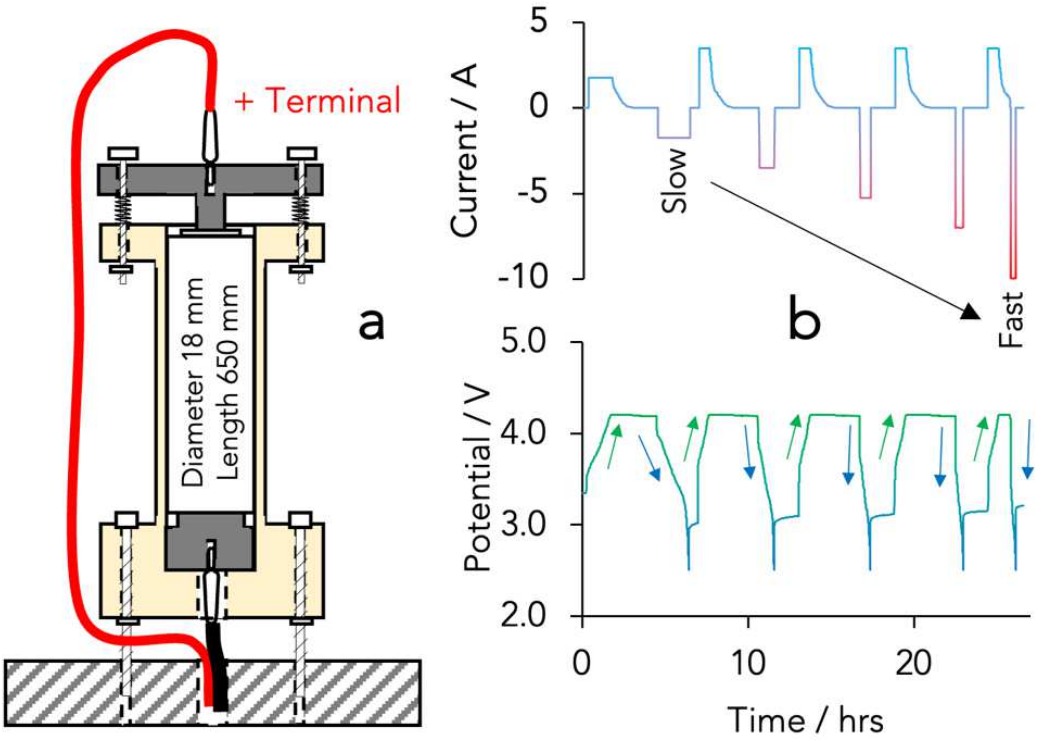

Fig S2. **Electrochemical cycling data collected using the operando cell holder. a,** A schematic image of the cell holder with electrical terminals (red/black) and 18650 cell. **b,** Electrochemical data obtained using the cell holder during characterisation at various C-rates.

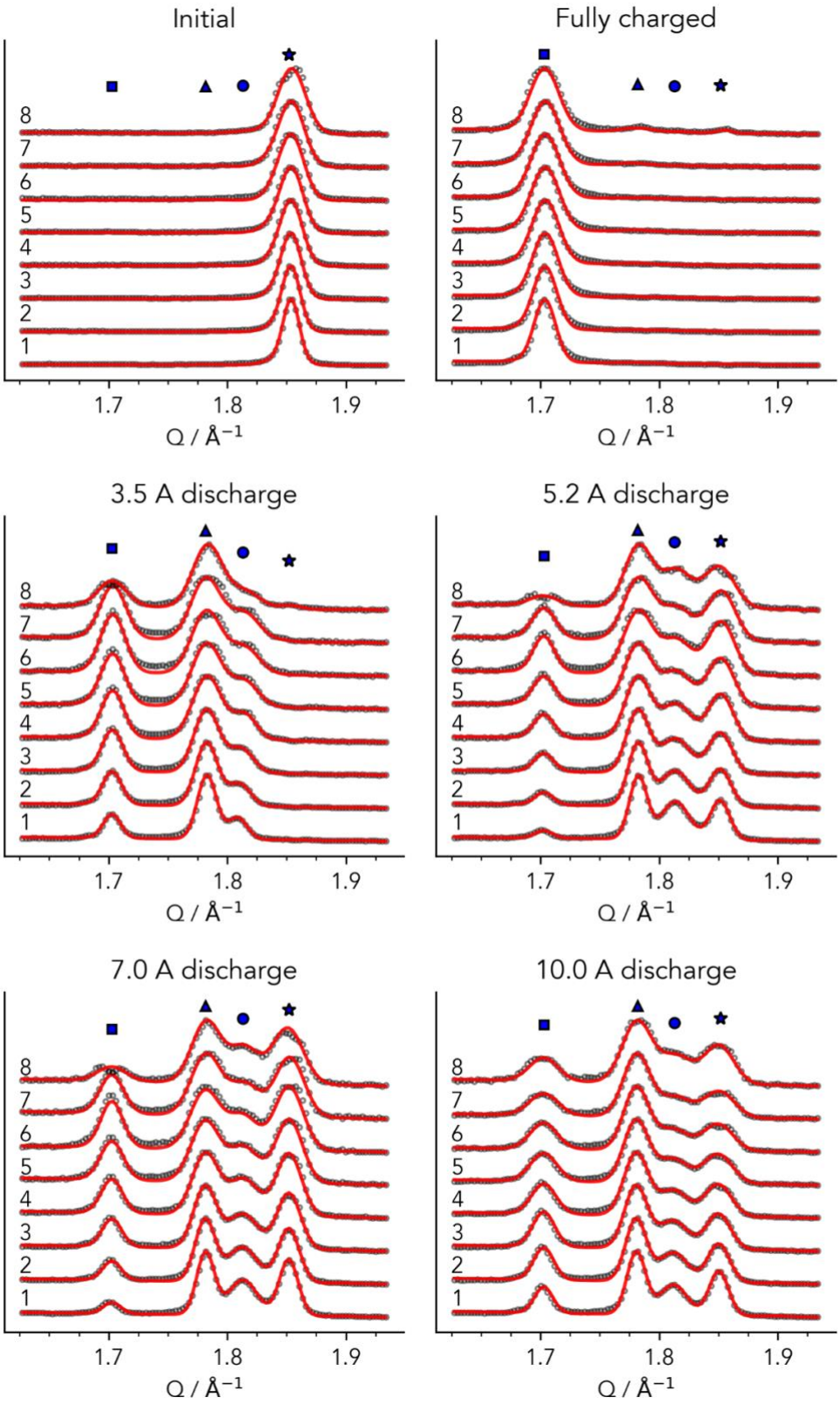

Fig S3. X-ray diffraction data collected on MJ1 cell using the operando cell holder for SoC calculations. Diffraction patterns for the 8 zones in which the battery volume was divided at initial discharged state, final charged state. For each current applied during discharge (3.5A, 5.25A, 7.0A, 10.0A) the patterns are shown at Li x= 0.5. It is possible to distinguish the four graphite stages and their distribution depending on the discharge current applied.

Fig. S4a shows the Ewald's sphere construction and its relation to the scattering vector defined as Q = k_s- k_i, where k_i denotes the incoming and k_s the outgoing wave vectors. As a reference, the beam direction is on *x* axis and vertical rotation is on *z* axis. Diffraction occurs, whenever the sphere, representing all the possible orientation of G_{hkl} reciprocal space vector, intercepts the Ewald's sphere; In case of an anisotropic deformation, the sphere became an ellipsoid (**Fig. S4b**). When the battery cycles, the components, such as the current collector, suffer of an anisotropic deformation. In this case the powder diffraction rings are the result of the intersection between the Ewald's sphere and the strain ellipsoid. The interception of the axial strain and the Ewald's sphere during rotation around the tomographic *z* axis is constant. The vertical scattering component can be used to tomographic reconstruct the axial strain in the sample. On the contrary, as shown in **Fig. S4c** the intersection of the Ewald's sphere and the strain in the horizontal plane is not invariant for rotation around the tomographic *z* axis. As a consequence, the horizontal scattering component can not be used for strain tomographic reconstructions.

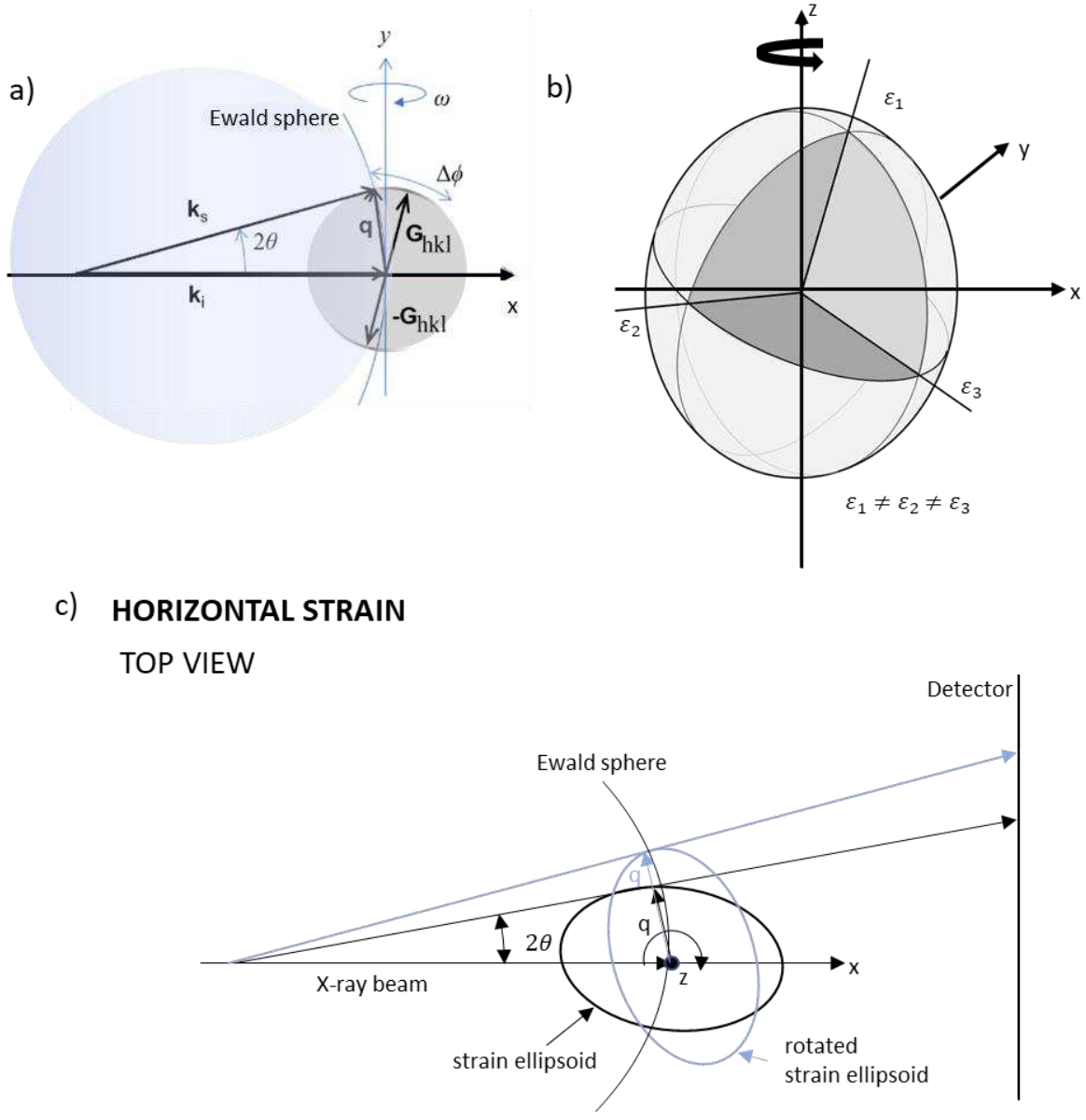

Fig S4. Strain components. a, Ewald's sphere construction and its relation to the scattering vector. **b,** Ewald's sphere in the case of an anisotropic deformation, the sphere becomes an ellipsoid. **c,** Intersection of the Ewald's sphere and the strain in the horizontal plane.

It was found that non-vertical components displayed a complicated distribution of strain. This is visualised in **Fig S5a** whereby the cell is examined via a horizontal cross-section (analogous to that seen in **Fig. 1**) at approximately half of the cell's vertical height that is divided into 8 rings as was employed in **Fig. 2** (the 1st ring at the cell wall and the 8th at the cell core). Considering the radial zone-to-zone variation (**Fig. S5b**) revealed a strain inflection point towards the cell core (around zones 6 and 7 in **Fig. S5c**). Correlating this observation to the laboratory attenuation X-ray CT revealed a misalignment of the electrode layers within the jellyroll (**Fig. S5d**). The electrode layers appear to shift vertically, most clearly near the base of the cell casing, with a distinct lack of electrode material within the strain 'inflection' zone (**Fig. S5f**) compared to either side of this zone where active material is visible (**Fig. S5e,g**,). This is perhaps even more evident by the shift in vertical alignment when viewed orthogonally (**Fig. S5h**). Moreover, this strain distribution appeared to be particularly severe when compared to an equivalent LFP-Gr cell (**Fig. S6**).

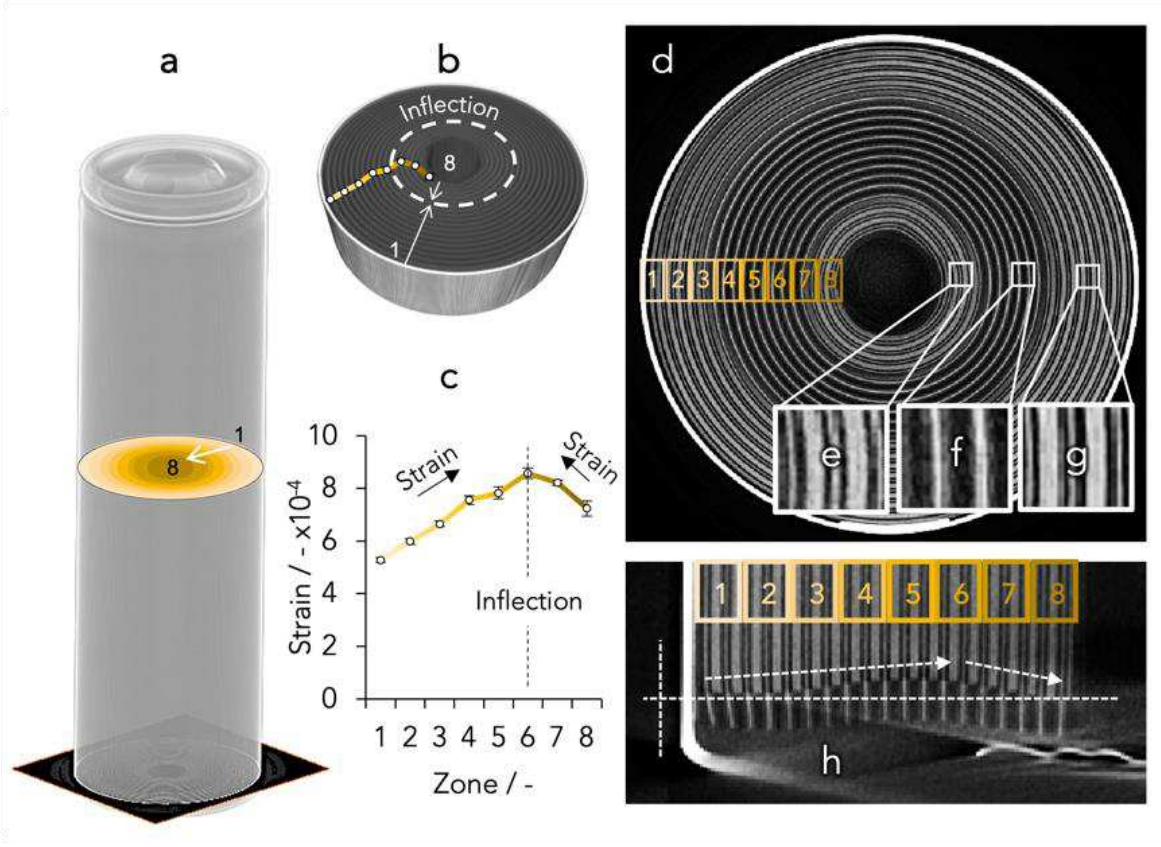

Fig. S5 **Resolving mechanical strain using XRD-CT**. **a,** Semi-transparent volume render of the 18650 cell with an indicating the spatial location of the cross-section. **b,c,** A sub-sectioned volume render of the cell indicating (b) the location and (c) the magnitude of the inflection point feature. **d,e,f,g,** A horizontal greyscale ortho-slice cross-section taken near the cell base as indicated in (a), with reference to three magnified regions (e) before, (f) during and (g) after the inflection. **h,** Another greyscale ortho-slice taken but in the orthogonal (vertical) plane.

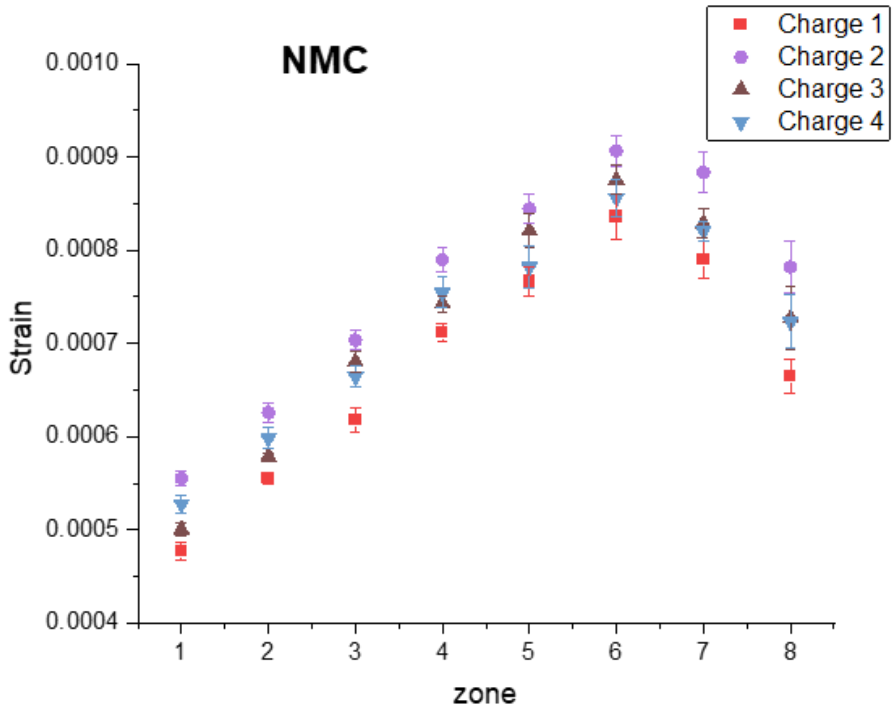

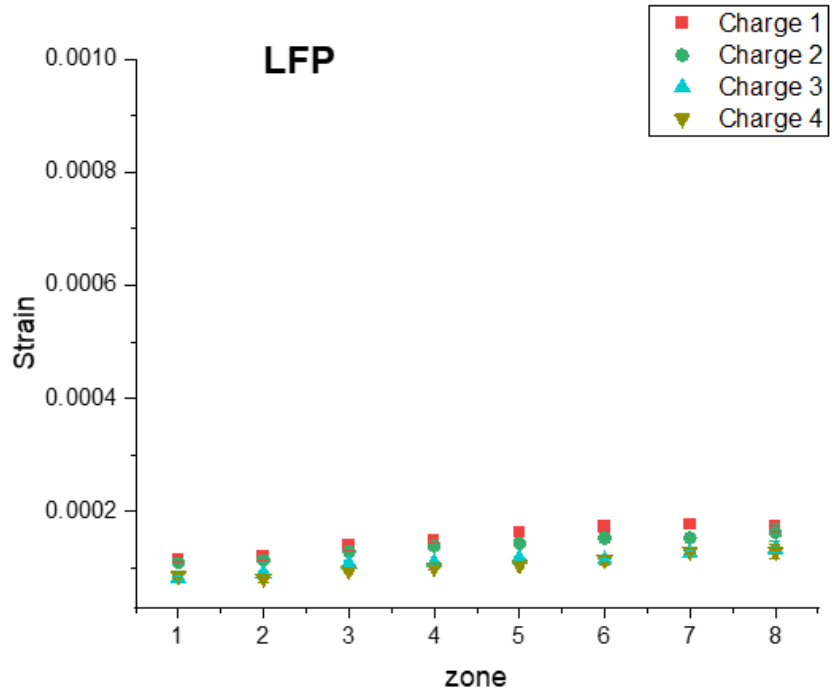

Fig S6. Vertical strain components after charge of 18650 cells. The vertical strain component calculated on the two 18650 cells (NMC and LFP) from the Cu d-spacing difference before and at the end of repeated charges at 1C rate after 1h relaxation. Multiple 1C charges were compared to understand the influence of successive cycles. The cell volume was again divided in 8 circular zones to understand the strain variation distribution inside the battery. **a,** shows strain on Cu current collector d-spacing at the end of 1C charges as a function of 8 circular zones inside an NMC cell. **b,** shows strain on Cu current collector d-spacing at the end of 1C charges as a function of 8 circular zones inside an LFP cell. Notice the strain caused by volume change during graphite silica composite anode lithiation is some orders higher than LFP cell graphite lithiation.

Fig. S7 displays the NMC811 vs. Gr-SiO_i cell which has a standard discharge rate of 0.2C and maximum discharge rate limited to 10 A (> 2C). We were therefore testing the full range of the cell's specified rate limits. The cell capacity exceeded the manufacturer's specification (>3.4 Ah) until 2C, after which a small decline in accessible discharge capacities was observed (ca. 3.2 Ah). Within commercial cells, the anode is often oversized to avoid capacity loss via a loss of lithium inventory. It is therefore common to not fully delithiate the anode during discharge. However, the degree of delithiation would be expected to be relatively uniform throughout the cell, XRD analysis revealed information contrary to this (**Fig. S8**).

Non-uniform strain distributions are important when considering SoC disparities; although there were subtle indications of charge balancing (see **Fig. S8**), the bulk SoC appeared homogenous when quantified during operation (**Fig. S9**). However, by dividing the cell into two sections: outside (**Fig. S7a**) and inside (**Fig. S7b**) of the strain inflection, a spatial distribution of the SoC showed a distinct correlation (**Fig. S7c**). Exploring this further with the inclusion of a range of discharge C-rates revealed a consistent disparity in SoC either side of the strain inflection most notably at the top (**Fig. S7d,f,h,j**) and bottom (**Fig. S7e,g,i,k**) of charge. Error bars indicate variation within the two radial zones. Curiously, C-rate does not appear to have an impact on the degree of SoC disparity between the two zones although, as would be expected due to the elevated overpotentials at higher C-rates, the extent of delithiation upon discharge decreases with increasing discharge rate. Comparing the impact of discharge rate and the disparity between the two radial zones: after discharge, the SoC within internal radial zone at 0.5C is comparable to the SoC within the external zone at 1.0C; the same conclusion can be drawn between 1.0C and 2.0C. Hence, the extent of anode delithiation during discharge appears to be impacted as severely by this strain inflection as doubling the cell C-rate, which is a substantial observation.

Resolving strain is important for the MCC experiments because the focal point of the data acquisition should be collected in a region with known strain values e.g., the 'strain-free' inflection point in this work (**Fig. S5c**). And although not the focus of this article, future work could explore the distribution of strain and the impact of accessible capacity within various 18650 cells using this method.

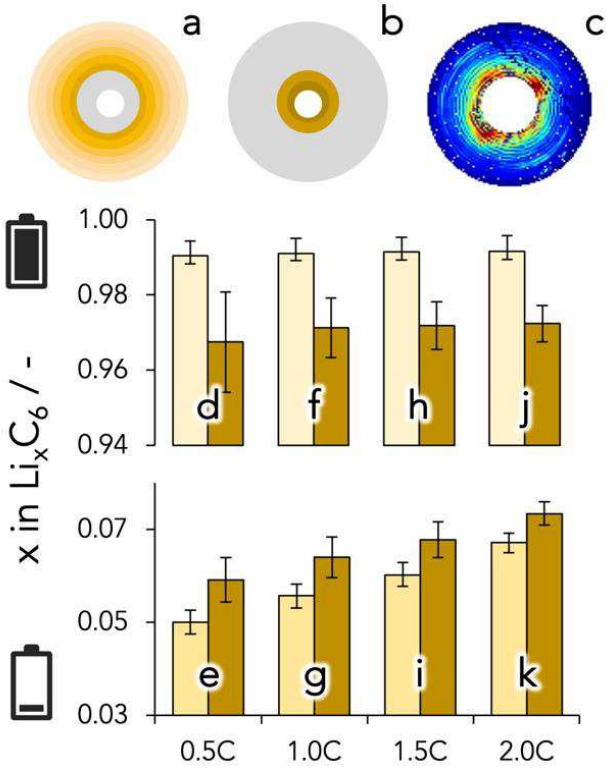

Fig. S7 **Resolving SoC using XRD-CT**. **a,b,c,** Cross-sections of the cell as schematics of the (a) the outer and (b) the inner zones, and (c) an XRD-CT heatmap of the local SoC for qualitative purposes. **d-k,** The extent of lithiation by quantifiying the x in LixC6 for the inner (light gold) and outter (dark gold) regions at the (d,g,h,j) top and (e,g,i,k) bottom of charge for C-rates of (d,e) 0.5C, (f,g) 1.0C, (h,i) 1.5C and (j,k) 2.0C.

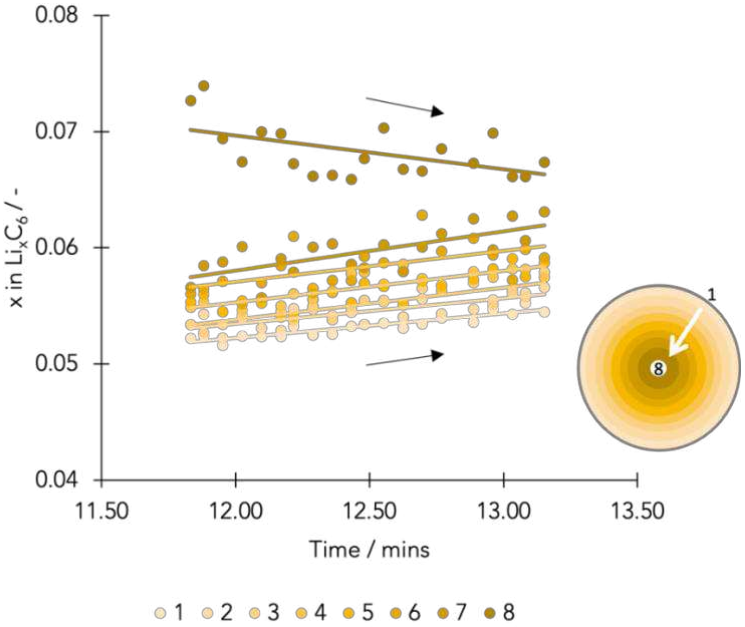

Fig S8. Degree of lithiation within the MJ1 18650 anode at the bottom of 1C discharge. Note: only a section of data is reported here displaying the lithiation states within the eight zones immediately after the 1C discharge.

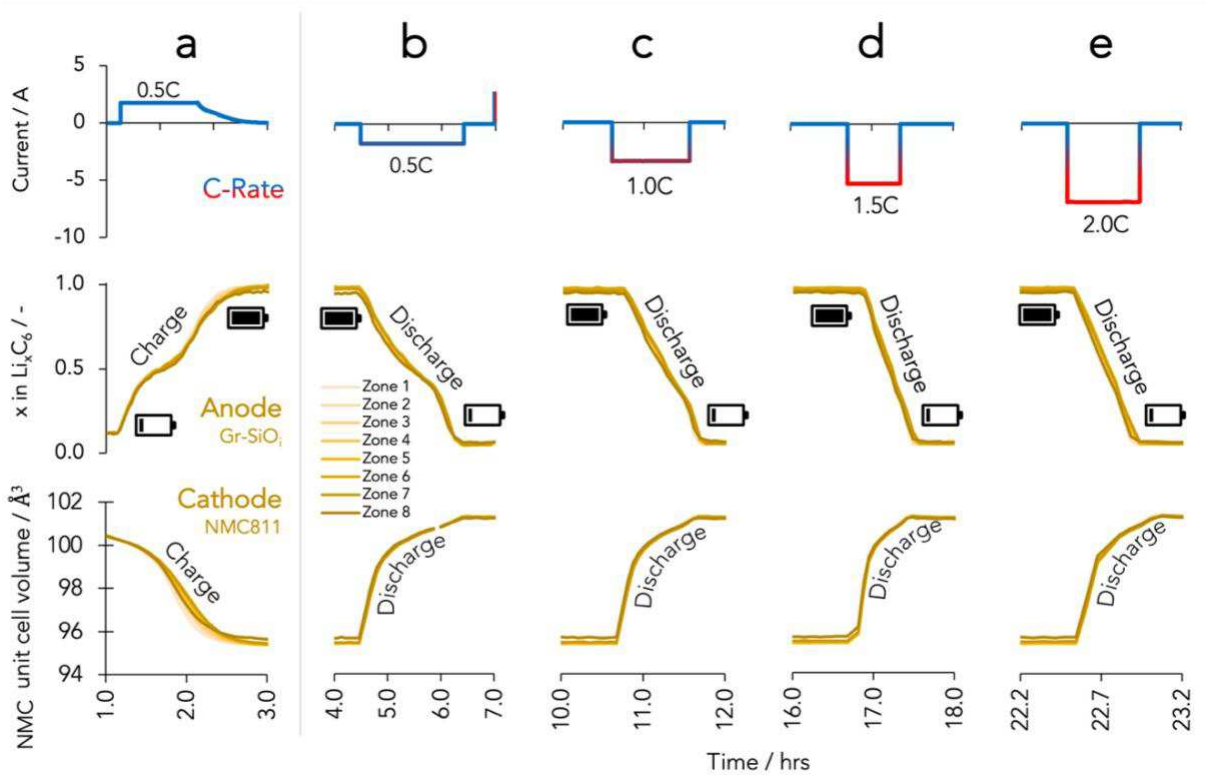

Fig 9. SoC quantifications within the MJ1 18650 at high-rates. The electrical current (top), anode lithiation (middle) and cathode unit cell expansion (bottom) for the first charge (a) and four subsequent discharges (d-e) at increasing C-rates.

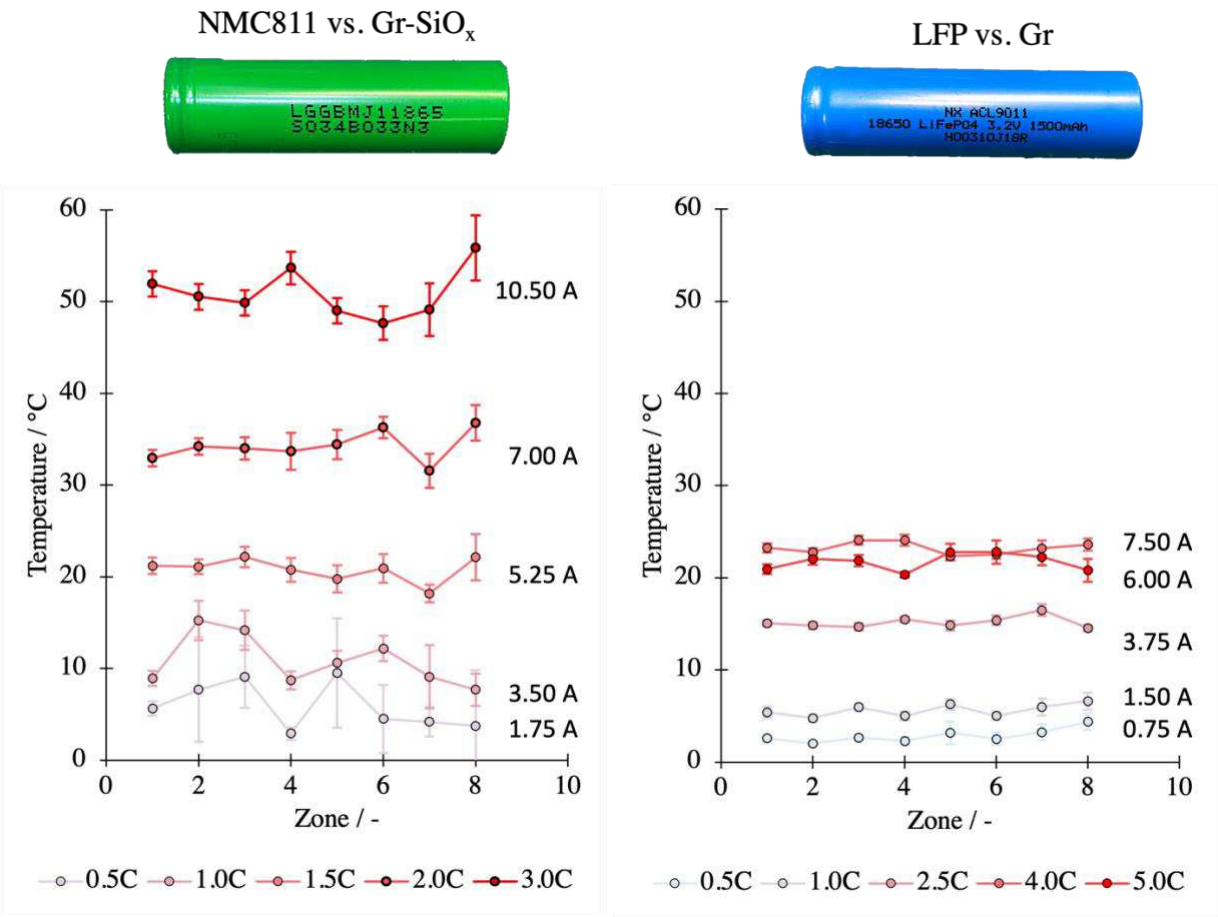

Fig S10. Comparing internal temperatures within the two 18650 cells. A repeat of the data presented in Fig. 2b obtained from the NMC cell, with comparison to the LFP cell. Radial zones are shown. All temperature values are reported as the temperature difference between a point in the cell and the ambient temperature.

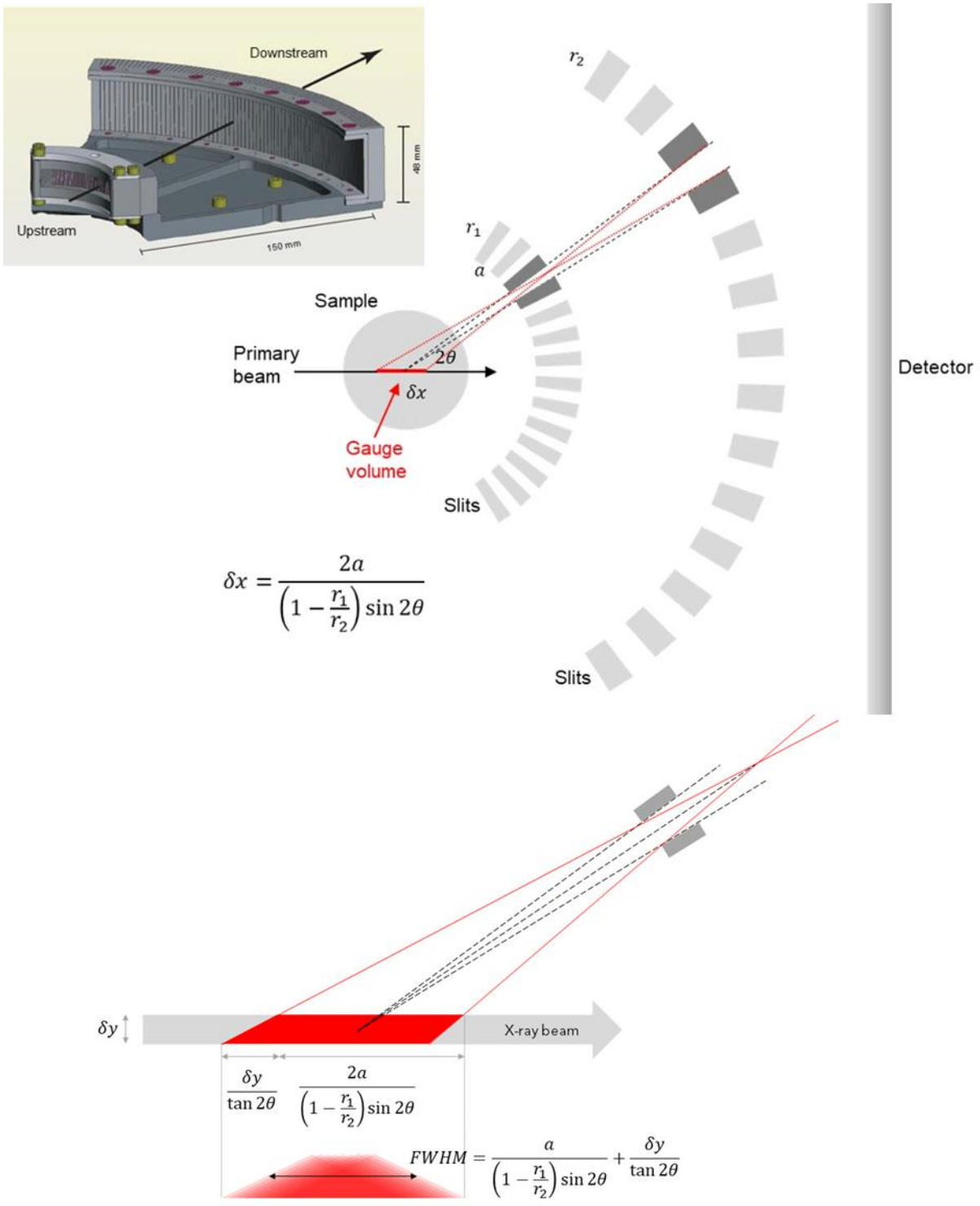

Fig S11. **Top,** schematic and working principle of the multi channel collimator (MCC) used for operando experiments adapted from [28,29]. The expression for the length of the gauge volume, δx, is given as a function of inner and outer slit radii (r_1, r_2) and scattering angle (2θ). **Bottom,** detail of the gauge volume indicated in the top panel, along with the expressions for gauge volume dimensions in the case of a primary beam of width δy; r_1, r_2, and 2θ have the same meaning as in the panel above.

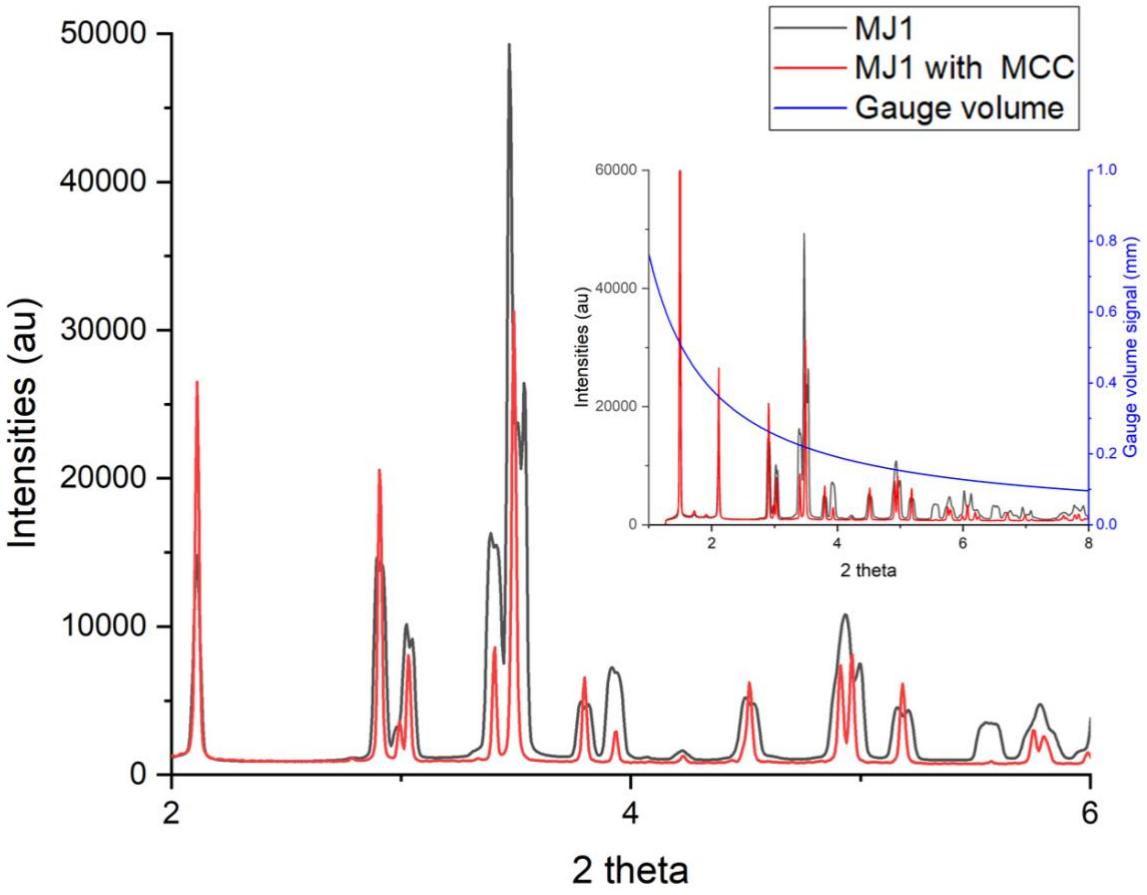

Fig S12. Comparison of MJ1 diffraction patterns obtained without the MCC (black), and with the MCC (red). Inset: full range of the MJ1 diffraction patterns with and without MCC, along with the calculated intensity from the gauge volume selected with the MCC.